

# Realization of a Synthetic Hall Torus with a Spinor Bose-Einstein Condensate

T. -H. Chien,<sup>1</sup> S. -C. Wu,<sup>1</sup> Y. -H. Su,<sup>1</sup> L. -R. Liu,<sup>1</sup> N. -C. Chiu,<sup>1</sup> M. Sarkar,<sup>2</sup> Q. Zhou,<sup>3,\*</sup> and Y. -J. Lin<sup>1,4,†</sup>

<sup>1</sup>*Institute of Atomic and Molecular Sciences, Academia Sinica, Taipei, Taiwan 10617*

<sup>2</sup>*Department of Physics, University of Mumbai, Mumbai 400098, India*

<sup>3</sup>*Department of Physics and Astronomy, Purdue University, West Lafayette, IN 47907-2036, USA*

<sup>4</sup>*Department of Physics, National Tsing Hua University, Hsinchu 30013, Taiwan*

(Dated: February 17, 2026)

We report the first experimental realization of a synthetic Hall torus using a spinor Bose-Einstein condensate confined in a ring-shaped trap with *in situ* imaging. By cyclically coupling three hyperfine spin states via Raman and microwave fields, we impose a periodic boundary condition in the synthetic dimension, which—together with a real-space ring trap—realizes a toroidal geometry with a synthetic magnetic flux. This flux induces azimuthal density modulations in the condensate, whose periodicity is uniquely determined by the quantized toroidal magnetic flux—a hallmark of the Hall torus geometry. By varying the relative phase between the couplings across repeated experimental runs, we control the location of the density extrema, emulating the behavior of Thouless charge pump in a toroidal geometry. We further investigate the onset of these modulations as the system transitions from a cylindrical to a toroidal topology. Our results establish a versatile platform for investigating quantum Hall physics and topological phenomena in synthetic curved spaces.

The development of synthetic dimensions [1–6] using internal atomic states opened new pathways for simulating higher-dimensional physics and implementing unconventional boundary conditions. In addition to hyperfine spin states [7–18], other degrees of freedom including momentum modes [19–23], vibrational states [24, 25], and Rydberg atom arrays [26, 27] have also been employed, enriching the experimental toolbox for physicists to control synthetic quantum matter. These advances have enabled the observation of exotic quantum phenomena, such as chiral edge transport and nontrivial band topology, in highly tunable systems. Notably, the introduction of periodic boundary conditions in the synthetic dimension has made it possible to construct novel geometries that are not easy to access in conventional approaches. Prototypical examples include synthetic cylinders and tori, where magnetic fluxes can be threaded through closed surfaces, circumventing the limitations of real-space implementations. A theoretical framework for such geometries was introduced in Ref. [17], predicting rich band structures and symmetry-protected features. A few experiments have successfully demonstrated synthetic Hall cylinders in laboratories [11, 13–16], laying the groundwork for the realization of more complex topological structures.

The Hall torus provides a fundamentally important platform for exploring quantum phenomena in curved and topologically nontrivial spaces. A toroidal geometry introduces conceptually new features in quantum many-body physics that are unattainable in planar systems. For instance, topological order, which is characterized by ground state degeneracy robust to local disturbance, emerges in fractional quantum Hall states on a torus [28]. These degenerate states are indistinguishable by any local observable but are globally distinct due to long-range quantum entanglement, reflecting the presence of non-

trivial anyonic excitations and braiding statistics [29]. These features make the Hall torus an ideal setting for probing the interplay between geometry, topology, and quantum coherence. However, the Hall torus has remained experimentally elusive. The absence of magnetic monopoles in nature prevents the threading of a magnetic flux through a closed toroidal surface, posing a fundamental obstacle to realizing a Hall torus in real space. As a result, experimental studies of Hall physics have largely been confined to planar geometries or extended to cylindrical systems [7–16]. While these systems have revealed rich physics, ranging from edge states to topological charge pumping, they lack the closed topology of a true torus. It is therefore desirable to realize a synthetic Hall torus that can simultaneously emulate both the geometry and the gauge field configuration within a highly controllable quantum system.

In this Letter, we report the first experimental realization of a synthetic Hall torus using an atomic  $F = 1$  spinor Bose-Einstein condensate confined in a ring-shaped potential. The synthetic dimension is encoded in the three magnetic sublevels  $m_F = \pm 1, 0$ , and cyclic coupling among them is implemented via a combination of Raman and microwave fields. This cyclic coupling imposes a periodic boundary condition in the synthetic dimension, which, together with the ring trap in real space with radius  $R \sim 14 \mu\text{m}$ , constructs a toroidal geometry (see Fig. 1b). To emulate a Hall torus, we create a synthetic magnetic field penetrating the toroidal surface using a Raman coupling that simultaneously changes the spin state  $m_F$  and the center-of-mass orbital angular momentum (OAM) of the atoms. This scheme imparts a net OAM transfer of  $\Delta\ell = 2\hbar$  within the same spin state and thus coherent interference of wavefunctions of different OAM. As a hallmark of the Hall torus, we adopt *in situ* imaging to observe a characteristic den-

sity modulation with two distinct minima (or maxima) along the azimuthal direction of the ring—an effect absent when the microwave coupling is turned off, leaving the synthetic dimension with open boundary conditions. By tuning the relative phase between the microwave and Raman fields cross repeated experimental runs, we gain control over the azimuthal position of the density modulation, thereby mimicking a topological charge pump on a torus. Furthermore, by exploiting the tunability of atom–laser interactions, we dynamically switch the boundary condition in the synthetic dimension and investigate the nonequilibrium emergence of density modulations as the system acquires toroidal topology.

We start from a description of our setup and the Hamiltonian. We implement the Raman coupling using a pair of laser beams copropagating along  $\mathbf{e}_z$ : a Gaussian beam and a Laguerre-Gaussian (LG) beam with phase winding number 1, thus carrying OAM of  $\hbar$ . These beams couple bare spin states  $|m_F\rangle$  to  $|m_F \pm 1\rangle$ , transferring  $\pm\hbar$  of OAM (Fig. 1c). The resulting Raman coupling strength has an approximately cylindrically symmetric spatial profile  $\Omega(r) = \Omega_M \sqrt{e}(r/r_M) e^{-r^2/2r_M^2}$ , where  $r_M$  is the radial position of maximum coupling. The nonuniform spatial profile  $\Omega(r)$  creates a spatially varying light shift that concentrates atoms near  $r_M$  in the radial direction, thereby producing an effective ring-shaped trapping potential. Such ring traps were previously implemented for studying superflows in BECs and spin-orbit-angular-momentum coupling [30–36]. In our setup,  $\Omega_M/2\pi = 3.8$  kHz and  $r_M = 17\ \mu\text{m}$ . The Raman detuning is given by  $\delta = \Delta\omega_L - \omega_Z$ , where  $\Delta\omega_L$  is the frequency difference between the two beams and  $\omega_Z$  is the effective linear Zeeman shift. Additionally, we apply a two-photon microwave field to resonantly couple  $|m_F = 1\rangle$  and  $|m_F = -1\rangle$  with a strength  $\Omega_{\text{mw}}/2\pi = 3.15 \pm 0.25$  kHz. The total atom–light coupling Hamiltonian in the coordinate  $(r, \phi, z)$  at  $\delta = 0$  reads:

$$V/\hbar = \frac{\Omega(r)}{\sqrt{2}} e^{i\phi} |1\rangle\langle 0| + \frac{\Omega(r)}{\sqrt{2}} e^{i\phi} |0\rangle\langle -1| + \frac{\Omega_{\text{mw}}}{2} e^{-i\theta_{\text{mw}}} | -1\rangle\langle 1| + \text{H.c.} - \omega_q |0\rangle\langle 0|, \quad (1)$$

where  $\omega_q$  is the effective quadratic Zeeman shift. Both  $\omega_Z$  and  $\omega_q$  include light shifts from the microwave field (see Supplemental Materials). The value of  $\omega_q/2\pi$  is 1.6 kHz (50 Hz) for  $\Omega_{\text{mw}}/2\pi = 3.15$  kHz (0). The microwave phase  $\theta_{\text{mw}}$  is actively locked to the relative phase of the Raman beams, ensuring reproducible and tunable node positions of the density modulations. The transition from  $| - 1\rangle$  to  $| 0\rangle$  and that from  $| 0\rangle$  to  $| 1\rangle$  carry a phase factor  $e^{i\phi}$  dependent on the azimuthal angle  $\phi$  of the ring. The transition from  $| 1\rangle$  to  $| - 1\rangle$  carries a constant phase  $-\theta_{\text{mw}}$ , leading to a position-independent flux  $-\theta_{\text{mw}}$  through the cross section, as analogous to the flux along the axial direction in a Hall cylinder. Therefore, the total flux penetrating the toroidal surface is  $2(\phi_0 + 2\pi) - 2\phi_0 = 4\pi$

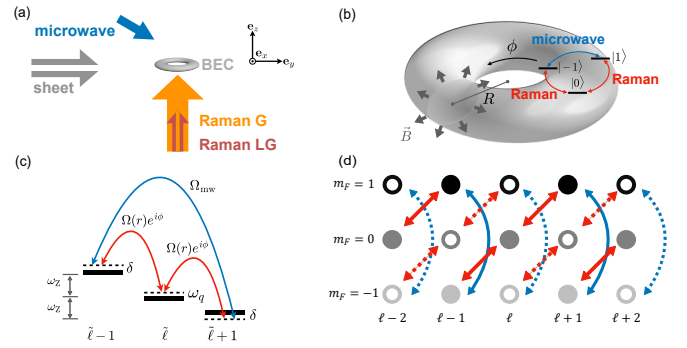


FIG. 1: (a) Experimental setup. (b) The torus combines a ring trap in real space with cyclically coupled spin states in the synthetic dimension. (c) Schematic of the cyclic coupling implemented by Raman (red) and microwave fields (blue). (d) Cyclic coupling displayed in the spin and OAM space. Solid (open) symbols denote atoms in torus branch 1(2).

for arbitrary  $\phi_0$ .

The atom–light interaction in Eq.(1) gives rise to a unique feature of the eigenstates in the azimuthal direction. Using  $|m_F, l\rangle \propto e^{il\phi}$  to denote the state with spin  $m_F$  and OAM  $l$  in unit of  $\hbar$ , these states are coupled by (1) via the sequence  $\dots | -1, l = \ell \rangle \leftrightarrow | 0, \ell + 1 \rangle \leftrightarrow | 1, \ell + 2 \rangle \leftrightarrow | -1, \ell + 2 \rangle \dots$  as shown in Fig. 1d. The eigenstates are thus grouped into two branches that remain decoupled under cylindrical symmetry, which are denoted by filled (branch 1) and hollow (branch 2) circles, respectively, in Fig. 1d. Both the eigenstates of branch 1 and 2 are labeled by quasi-OAM  $\ell$ . The eigenstate of branch 1, 2 are

$$|\Phi_1\rangle = \sum_{m_F=0,\pm 1} \sum_{n=-\infty}^{\infty} c_{1,m_F,n} |m_F, \ell + m_F + 2n\rangle, \quad (2a)$$

$$|\Phi_2\rangle = \sum_{m_F=0,\pm 1} \sum_{n=-\infty}^{\infty} c_{2,m_F,n} |m_F, \ell + m_F + 1 + 2n\rangle, \quad (2b)$$

where  $c_{1,m_F,n}$  and  $c_{2,m_F,n}$  characterize the weight of each OAM state in this superposition. Since the kinetic energy scales as  $l^2\hbar^2/2MR^2 = l^2E_0$  where  $E_0 \approx \hbar \times 0.3$  Hz is much smaller than  $\Omega_{\text{mw}}$  and  $\Omega_M$ , each  $|m_F\rangle$  has multiple OAM states. For each  $|m_F\rangle$ , the angular momenta are equally spaced with a spacing of  $d_\phi = 2$ , analogous to the reciprocal lattice vector in a linear lattice. As such, each  $|m_F\rangle$  has a periodic lattice structure of a lattice space  $2\pi/d_\phi = \pi$  in the azimuthal direction. The two-dimensional density thus oscillates as  $n_{m_F}^{2\text{D}}(r, \phi) = n_{m_F}^{2\text{D}}(r, \phi + \pi)$ , exhibiting two maxima and two minima around the ring. In sharp contrast, without turning on the microwave coupling, each  $|m_F\rangle$  is associated with a single OAM  $l$  and the density modulation vanishes. Another notable feature is that  $\theta_{\text{mw}}$  determines the locations of the two maxima (minima). This can be

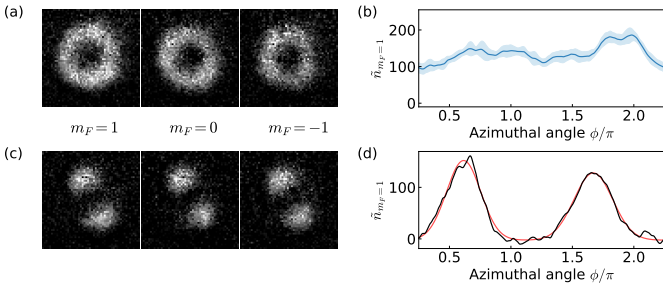


FIG. 2: Atomic optical density (OD) of  $|m_F = 1, 0, -1\rangle$  before turning on the microwave coupling  $\Omega_{\text{mw}}$  (a) and after turning on  $\Omega_{\text{mw}}$  in 50 ms with  $\theta_{\text{mw}} = 0$  and  $t_h \lesssim 0.1$  ms (c). The color scale for the density profile is given by the maximum value in each panel. The field of view is  $72 \times 72 \mu\text{m}^2$ . Azimuthal profiles of the ring (b) and torus (d) are displayed as the effective 1D density  $\tilde{n}_{m_F=1}$  vs.  $\phi$ . (b) shows the average and standard deviation of 10 identical experimental realizations. Black (red) curve in (d) denotes the experimental data (fit). The images in (a) and (c) are single-shot.

directly seen from Eq.(1) that a gauge transformation  $|1\rangle \rightarrow e^{i\theta_{\text{mw}}/2}|1\rangle$ ,  $| - 1\rangle \rightarrow e^{-i\theta_{\text{mw}}/2}| - 1\rangle$  eliminates the phase of the coupling  $| - 1\rangle\langle 1|$  while modifying phases of the couplings  $|1\rangle\langle 0|$  and  $|0\rangle\langle -1|$  to  $e^{i(\phi - \theta_{\text{mw}}/2)}$ . Consequently, physical quantities like  $n_{m_F}^{2\text{D}}$  are expressed as functions of  $\phi - \theta_{\text{mw}}/2$ . To focus on the azimuthal distribution of the density, we defined an effective 1D density  $\tilde{n}_{m_F}(\phi - \theta_{\text{mw}}/2) \propto \int dr n_{m_F}^{2\text{D}}(r, \phi - \theta_{\text{mw}}/2)$ . The locations of the maxima (minima) of  $\tilde{n}_{m_F}$  are therefore controlled by  $\theta_{\text{mw}}$ .

Our experiment begins with  $^{87}\text{Rb}$  atoms in  $|F = 1, m_F = -1\rangle$  state confined in a crossed optical dipole trap combined with a blue-detuned sheet potential. To initialize the system, we prepare cold thermal atoms and adiabatically load them into the lowest energy spinor branch Raman-dressed state  $|\xi_{-1}\rangle$  [35] by ramping on the Raman coupling over 10 ms while holding the detuning fixed at  $\delta_i/2\pi = 2.8$  kHz, followed by a linear ramp of  $\delta$  to zero over 40 ms. After loading, the atoms have temperature  $T \gtrsim T_c$ , where  $T_c$  is the BEC critical temperature. Evaporative cooling is then performed by gradually reducing the dipole trap power to near zero over 0.3 s, yielding a condensate of  $N = (8 \pm 1) \times 10^4$  atoms in the Raman-dressed state  $\varphi(\vec{r})|\xi_{-1}\rangle = \varphi(\vec{r}) \left( e^{i\phi \frac{1-\cos\beta}{2}}, -\frac{\sin\beta}{\sqrt{2}}, e^{-i\phi \frac{1+\cos\beta}{2}} \right)^T$ , where  $\varphi(\vec{r})$  is the external part of the condensate wave function, and  $\tan\beta = \Omega(r)/\delta$ . For our experiment with  $\delta = 0$ , the internal spinor state  $|\xi_{-1}\rangle$  has components  $(0.5, -\sqrt{0.5}, 0.5)$  in the ring-shaped trapping potential created by the dressed state light shift, approximately  $-\Omega(r)$  (see Supplemental Materials). In addition, the crossed dipole trap provides transverse confinement with  $\omega_r/2\pi = 25$  Hz, and the trap frequency along  $z$  is about 370 Hz.

In the ideal situation where the ring trap is per-

fectly cylindrically symmetric,  $\varphi(\vec{r})$  contains only a single Fourier component  $\ell_j = 0$ , and  $\tilde{n}_{m_F}$  is thus a constant in the ring trap before turning on the microwave field. In practice, however, the ring trap is not perfectly cylindrically symmetric and exhibits azimuthal roughness, primarily due to imperfect alignment between the Raman beams and the condensate. This roughness introduces additional Fourier components with  $\ell_j \neq 0$  such that  $\varphi(\vec{r}) \approx \sum_j a_j e^{i\ell_j \phi}$ , where small but finite  $a_{j \neq 0}$  makes the density no longer constant in the azimuthal direction. Another factor is that the 0.3 s evaporation duration may be not sufficiently long compared to  $(E_0/h)^{-1} \sim 3.3$  s where  $E_0$  is the smallest single-particle trap energy scale; hence, some atoms may not fully reach to the absolute ground state with  $\ell_j = 0$ . Both effects result in azimuthal density modulations that are too small to produce nodes. As shown in Fig 2(ab), we take *in situ* spin-selective imaging by abruptly switching off the Raman and microwave couplings, along with the dipole trap, after a brief 0.5 ms time-of-flight. The atomic optical density (OD) distribution for each  $|m_F\rangle$  component exhibits a ring-shaped profile with radii of  $\sim 14 \mu\text{m}$ .  $OD_{m_F}$  is given by  $n_{m_F}^{2\text{D}} \bar{\sigma}$ , where  $\bar{\sigma}$  is the imaging cross section. With  $\delta = 0$ , the spinor population fractions are approximately 0.25 in  $m_F = \pm 1$  and 0.5 in  $m_F = 0$ . Figure 2(b) shows that nodes are absent in  $\tilde{n}_{m_F}(\phi)$ , though a small density variation exists due to the aforementioned imperfections, suggesting that cylindrical symmetry breaking factors do not significantly restructure the density profiles.

To engage the cyclic coupling, we ramp on the two-photon microwave coupling  $\Omega_{\text{mw}}$  over a time  $t_{\text{on}}$  with a defined phase  $\theta_{\text{mw}}$ , while simultaneously adjusting the bias magnetic field by 2.1 kHz to compensate for the microwave-induced light shift, thereby maintaining  $\delta \approx 0$  during  $0 \leq t \leq t_{\text{on}}$ . After a variable hold time  $t_h$ , we perform *in situ* imaging. Figure 2(cd) shows that with  $t_{\text{on}} = 50$  ms,  $\theta_{\text{mw}} = 0$  and  $t_h \lesssim 0.1$  ms, the atomic OD exhibits two depleted regions along the azimuthal direction  $\phi$ , where the density is suppressed down to zero, and correspondingly two maxima in the density profile, signifying the profound density modulation induced by the toroidal geometry. We characterize the evolution of the torus profile as a function of  $t_{\text{on}}$  with a short  $t_h \lesssim 0.1$  ms and find that the profile becomes largely unchanged for  $t_{\text{on}} \gtrsim 35$  ms. Accordingly, we adopt  $t_{\text{on}} = 50$  ms as the standard loading duration.

For general  $t_{\text{on}}$ , we compute  $\tilde{n}_{m_F=1}$  of the torus vs.  $\phi$  and fit it to a double Gaussian distribution function. We then extract the two peak locations  $\phi = \mu_1, \mu_2$  along with their root-mean-square widths, denoted  $\sigma_1$  and  $\sigma_2$ , respectively. For the standard  $t_{\text{on}} = 50$  ms with  $\theta_{\text{mw}} = 0$ , we repeat 10 identical experimental realizations and find  $\mu_1 = 0.62 \pm 0.02 \pi$  and  $\mu_2 = 1.69 \pm 0.02 \pi$ , with widths  $\sigma_1 = 0.135 \pm 0.02 \pi, \sigma_2 = 0.15 \pm 0.01 \pi$ ; see Fig. 2(cd). The separation  $\mu_2 - \mu_1 = 1.07\pi \sim \pi$  is consistent with the

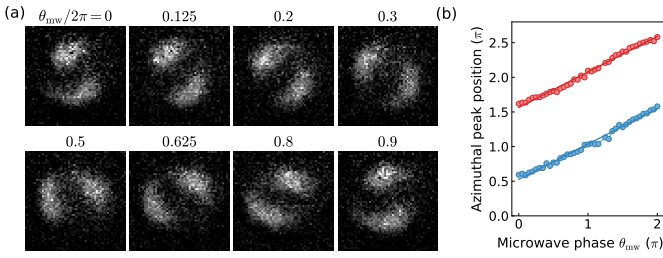


FIG. 3: (a) Atomic OD of  $|m_F = 1\rangle$  vs. microwave phase  $\theta_{\text{mw}}$  with  $t_{\text{on}} = 50$  ms and  $t_h \lesssim 0.1$  ms. The field of view is  $72 \times 72 \mu\text{m}^2$ . (b) Blue (red) symbols denote the azimuthal peak position  $\mu_1$  ( $\mu_2$ ) vs.  $\theta_{\text{mw}}$ . Lines denote the respective linear fits, both with slope  $0.51 \pm 0.01$ .

expected twofold azimuthal modulation of a torus. We also examine  $\text{OD}_{m_F=1}$  as a function of radial position  $r$  at the azimuthal peak locations  $\phi = \mu_1, \mu_2$ , and identify the corresponding radii of maximal OD as  $r = R_1$  and  $R_2$ . We find  $R_1 \sim R_2 = R = 14 \pm 1.5 \mu\text{m}$ . Although the torus profiles vary little for  $t_{\text{on}} \gtrsim 35$  ms, we observe small fluctuations of  $\mu_{1,2}$  by up to  $\sim 0.03 \pi$  and of  $\sigma$  by  $\sim 0.05 \pi$  over the range  $35$  ms  $\lesssim t_{\text{on}} \lesssim 80$  ms. The extracted  $R_{1,2}$  values in this range vary within the standard deviations of  $R$ .

In the ideal case of a perfectly cylindrically symmetric ring trap, only a single torus branch exists in Fig. 1(d), and the two maxima are identical. However, due to the imperfect ring trap and the finite evaporation time, a small mixing of the two branches exist, leading to a minor asymmetry between the two peaks of the torus. We analyze the different peak amplitudes and widths in  $\tilde{n}_{m_F=1}$ ,  $A_1 \neq A_2, \sigma_1 \neq \sigma_2$ , and the area ratio  $r_a = A_1\sigma_1/A_2\sigma_2$ . The areas are proportional to the atom numbers, and thus  $r_a$  is an indicator of asymmetry. We find that  $r_a = 1.1 \pm 0.1$  and  $A_1/A_2 = 1.2 \pm 0.2$  with  $\theta_{\text{mw}} = 0$ , showing a finite but relatively small mixing between two branches. The ratio  $r_a$  varies approximately between 0.7 and 1.4 for  $0 \leq \theta_{\text{mw}} \leq 2\pi$ . We notice day-to-day variations in the ring trap profile  $|\varphi(\vec{r})|^2$ , potentially due to drifts of beam misalignments and sheet potentials, while the branch mixing remains small with variations in  $r_a$  of up to 30% for a given  $\theta_{\text{mw}}$ . We further observe that the torus shape can vary slightly from day to day for a given  $\theta_{\text{mw}}$ , while the peak positions  $\mu_{1,2}$  remain stable within 1.5 standard deviations. Nevertheless, the density nodes in the torus always exist, indicating the robustness of the density modulations due to its topological origin in the toroidal geometry.

Whereas the appearance of the density modulation with two maxima readily signifies the creation of a synthetic Hall torus, we further control the locations of the maxima by tuning the microwave coupling phase  $\theta_{\text{mw}}$ . Since  $\theta_{\text{mw}}$  corresponds to the axial magnetic flux in the Hall cylinder [15, 16], introducing a time-dependent

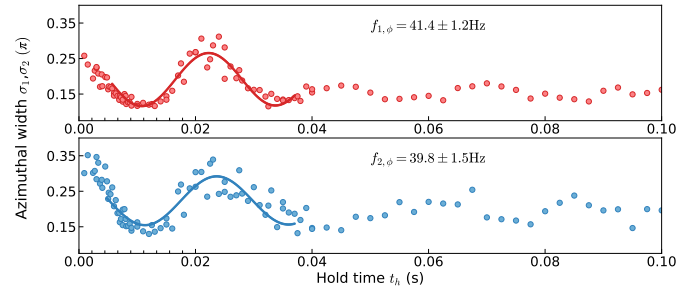


FIG. 4: Dynamics after a sudden transition from a cylindrical to a toroidal geometry by abruptly turning on  $\Omega_{\text{mw}}$ . Azimuthal widths  $\sigma_1, \sigma_2$  of the torus peaks centered at  $\phi = \mu_1, \mu_2$  vs. hold time  $t_h$  are displayed in the top and bottom panel, respectively.

$\theta_{\text{mw}}(t)$  that slowly varies would allow us to realize the topological charge pump on the torus similar to that in Ref. [16]. However, technical constraints in our setup limits us from slowly vary  $\theta_{\text{mw}}$  after a condensate is loaded to the torus. Instead, we repeat the same experiment for various  $\theta_{\text{mw}}$ . After finishing the aforementioned experimental procedures for a given  $\theta_{\text{mw}}$ , we choose a different  $\theta_{\text{mw}}$  and repeat the preparation of the Hall torus and the density measurements. This approach of monitoring the dependence of the density profile on  $\theta_{\text{mw}}$  thus mimics the topological charge pump on a Hall torus. Figure 3 shows  $\text{OD}_{m_F=1}$  as  $\theta_{\text{mw}}$  is varied from 0 to  $2\pi$ , and the peak positions  $\mu_1, \mu_2$  vs.  $\theta_{\text{mw}}$ . As expected, the azimuthal modulation rotates with  $\theta_{\text{mw}}$ :  $\mu_1$  and  $\mu_2$  increase linearly with  $\theta_{\text{mw}}$ , both with the slope of linear fit  $0.51 \pm 0.01$ . Once  $\theta_{\text{mw}}$  increases by  $2\pi$ , the location of each density maximum shifts by only  $\pi$ . To return each maximum to its original position,  $\theta_{\text{mw}}$  needs to change by  $4\pi$ . This behavior reflects the underlying nonsymmorphic symmetry of the synthetic Hall torus [17]. While the Hamiltonian is periodic in  $\theta_{\text{mw}}$  with a period of  $2\pi$ , as seen from Eq.(1) where  $V(\theta_{\text{mw}}) = V(\theta_{\text{mw}} + 2\pi)$ , the density modulation of each hyperfine spin state exhibits a period of only  $\pi$ . This reduced periodicity is a direct consequence of the nonsymmorphic symmetry and also underlies the formations of the so-called subwavelength lattices [13, 14, 18].

Since a condensate exhibits pronounced density modulations on a Hall torus that are absent in a cylinder geometry (open boundary condition for synthetic dimension), this motivates an exploration of how such density modulations arise as the boundary condition in the synthetic dimension is changed. To this end, we probe the post-quench dynamics, initiated by a short pulse ( $t_{\text{on}} = 0.01$  ms) that turns on the microwave coupling with  $\theta_{\text{mw}} = 0$ . In other words, we abruptly change the cylindrical geometry, which has an periodic and open boundary conditions in the real space (along  $\phi$ ) and the synthetic dimension, respectively, to a torus with periodic boundary conditions in both the real and the syn-

thetic dimensions. We then monitor  $\tilde{n}_{m_F=1}$  for hold times  $t_h$  up to 0.1 s by tracking the dynamics in the azimuthal direction. The initial  $\tilde{n}_{m_F=1}$  evolves into an azimuthal profile with two maxima where the two minima are nonzero. It takes  $t_h \sim 6$  ms for the density minimum to nearly deplete. Subsequently, the density distribution oscillates with  $t_h$ , since the initial density profile in the ring trap and that of the stationary eigenstate of a torus are distinct. In Fig. 4, we plot the azimuthal widths of the two peaks,  $\sigma_{1,2}$  vs  $t_h$ . In early times  $t_h \lesssim 0.04$  s, the oscillations of  $\sigma_1$  and  $\sigma_2$  are nearly sinusoidal, allowing us to extract their frequencies of  $41.4 \pm 1.2$  and  $39.3 \pm 1.5$  Hz. As  $t_h$  increases further, the oscillations deviate from a simple sinusoidal form and diminish in amplitude, indicating complex dynamics of the system approaching equilibrium after the quench (Supplemental Materials).

We have demonstrated the first experimental realization of a synthetic Hall torus, observed geometry-induced azimuthal density modulations, implemented a toroidal analogue of Thouless pumping, and probed dynamics following a sudden change in topology. Our approach provides a powerful platform for exploring quantum physics in curved spaces. While this work focuses on the weakly interacting regime, extending it to strongly interacting systems could enable fractional quantum Hall states and topological order on nontrivial manifolds. Moreover, the ability to dynamically tune topology and gauge fields opens exciting opportunities for investigating quantum transport and nonequilibrium topological phenomena.

The authors thank I. B. Spielman and C. -W. Chou for useful discussions. We also thank Y. Yan for valuable discussions and for kindly sharing Gross–Pitaevskii (GP) results on branch mixing and quench dynamics. Y. -J. L. was supported by NSTC 108-2112-M-001-033-MY3 and 111-2112-M-001-048-MY3 and the Thematic Research Program of Academia Sinica. Q. Z. was supported by the Air Force Office of Scientific Research under award number FA9550-20-1-0221.

---

\* Electronic address: [zhou753@purdue.edu](mailto:zhou753@purdue.edu)

† Electronic address: [linyj@as.edu.tw](mailto:linyj@as.edu.tw)

[1] O. Boada, A. Celi, J. I. Latorre, and M. Lewenstein, Phys. Rev. Lett. **108**, 133001 (2012).

[2] A. Celi, P. Massignan, J. Ruseckas, N. Goldman, I. B. Spielman, G. Juzeliūnas, and M. Lewenstein, Phys. Rev. Lett. **112**, 043001 (2014).

[3] T. Ozawa and H. M. Price, Nat. Rev. Phys. **1**, 349 (2019).

[4] A. Fabre and S. Nascimbene, EPL **145**, 65001 (2024).

[5] M. Buser, C. Hubig, U. Schollwöck, L. Tarruell, and F. Heidrich-Meisner, Physical Review A **102**, 053314 (2020).

[6] J. Argiello-Luengo, U. Bhattacharya, A. Celi, R. W. Chhajlany, T. Grass, M. Płodzień, D. Rakshit, T. Salamon, P. Stornati, L. Tarruell, et al., Communications Physics **7**, 143 (2024).

[7] B. K. Stuhl, H.-I. Lu, L. M. Aycock, D. Genkina, and I. B. Spielman, Science **349**, 1514 (2015).

[8] M. Mancini, G. Pagano, G. Cappellini, L. Livi, M. Rider, J. Catani, C. Sias, P. Zoller, M. Inguscio, M. Dalmonte, et al., Science **349**, 1510 (2015).

[9] T. Chalopin, T. Satoor, A. Evrard, V. Makhalov, J. Dalibard, R. Lopes, and S. Nascimbene, Nat. Phys. **16**, 1017 (2020).

[10] R. V. Roell, A. W. Laskar, F. R. Huybrechts, and M. Weitz, Phys. Rev. A **107**, 043302 (2023).

[11] J. H. Han, J. H. Kang, and Y. Shin, Phys. Rev. Lett. **122**, 065303 (2019).

[12] X.-W. Luo, J. Zhang, and C. Zhang, Phys. Rev. A **102**, 063327 (2020).

[13] C.-H. Li, Y. Yan, S.-W. Feng, S. Choudhury, D. B. Blasing, Q. Zhou, and Y. P. Chen, PRX Quantum **3**, 010316 (2022).

[14] R. P. Anderson, D. Trypogeorgos, A. Valdés-Curiel, Q.-Y. Liang, J. Tao, M. Zhao, T. Andrijauskas, G. Juzeliūnas, and I. B. Spielman, Phys. Rev. Res. **2**, 013149 (2020).

[15] Q.-Y. Liang, D. Trypogeorgos, A. Valdés-Curiel, J. Tao, M. Zhao, and I. B. Spielman, Phys. Rev. Res. **3**, 023058 (2021).

[16] A. Fabre, J.-B. Bouhiron, T. Satoor, R. Lopes, and S. Nascimbene, Phys. Rev. Lett. **128**, 173202 (2022).

[17] Y. Yan, S.-L. Zhang, S. Choudhury, and Q. Zhou, Phys. Rev. Lett. **123**, 260405 (2019).

[18] R. Zhang, Y. Yan, and Q. Zhou, Phys. Rev. Lett. **126**, 193001 (2021).

[19] E. J. Meier, F. A. An, and B. Gadway, Nat. Commun. **7**, 1 (2016).

[20] E. J. Meier, F. A. An, and B. Gadway, Phys. Rev. A **93**, 051602 (2016).

[21] D. Xie, T.-S. Deng, T. Xiao, W. Gou, T. Chen, W. Yi, and B. Yan, Phys. Rev. Lett. **124**, 050502 (2020).

[22] F. A. An, E. J. Meier, J. Ang'ong'a, and B. Gadway, Phys. Rev. Lett. **120**, 040407 (2018).

[23] W. Gou, T. Chen, D. Xie, T. Xiao, T.-S. Deng, W. Yi, B. Yan, and B. Gadway, Phys. Rev. Lett. **124**, 070402 (2020).

[24] G. Salerno, H. M. Price, M. Lebrat, S. Häusler, T. Esslinger, L. Corman, J.-P. Brantut, and N. Goldman, Physical Review X **9**, 041001 (2019).

[25] H. M. Price, T. Ozawa, and N. Goldman, Physical Review A **95**, 023607 (2017).

[26] S. K. Kanungo, J. D. Whalen, Y. Lu, M. Yuan, S. Dasgupta, F. B. Dunning, K. R. A. Hazzard, and T. C. Killian, Nature Communications **13**, 972 (2022).

[27] T. Chen, C. Huang, I. Velkovsky, K. R. A. Hazzard, J. P. Covey, and B. Gadway, Nat. Commun. **15**, 1 (2024).

[28] X.-G. Wen and Q. Niu, Physical Review B **41**, 9377 (1990).

[29] A. Y. Kitaev, Annals of physics **303**, 2 (2003).

[30] K. C. Wright, R. Blakestad, C. J. Lobb, W. D. Phillips, and G. K. Campbell, Physical review letters **110**, 025302 (2013).

[31] S. Eckel, J. G. Lee, F. Jendrzejewski, N. Murray, C. W. Clark, C. J. Lobb, W. D. Phillips, M. Edwards, and G. K. Campbell, Nature **506**, 200 (2014).

[32] K. Sun, C. Qu, and C. Zhang, Physical Review A **91**, 063627 (2015).

[33] L. Chen, H. Pu, and Y. Zhang, Physical Review A **93**, 013629 (2016).

[34] H.-R. Chen, K.-Y. Lin, P.-K. Chen, N.-C. Chiu, J.-B. Wang, C.-A. Chen, P. Huang, S.-K. Yip, Y. Kawaguchi, and Y.-J. Lin, Phys. Rev. Lett. **121**, 113204 (2018).

[35] P.-K. Chen, L.-R. Liu, M.-J. Tsai, N.-C. Chiu, Y. Kawaguchi, S.-K. Yip, M.-S. Chang, and Y.-J. Lin, Phys. Rev. Lett. **121**, 250401 (2018).

[36] D. Zhang, T. Gao, P. Zou, L. Kong, R. Li, X. Shen, X.-L. Chen, S.-G. Peng, M. Zhan, H. Pu, et al., Physical Review Letters **122**, 110402 (2019).

## Supplemental Materials of “Realization of a Synthetic Hall Torus with a Spinor Bose-Einstein Condensate”

### FORMALISM OF THE BEC DRESSED BY RAMAN AND MICROWAVE FIELDS

The Hamiltonian in the bare spin  $|m_F = 1, 0, -1\rangle$  basis under rotating wave approximation in the  $(r, \phi, z)$  coordinate is

$$\hat{H} = \left[ \frac{-\hbar^2}{2m} \frac{\partial}{r \partial r} (r \frac{\partial}{\partial r}) - \frac{\hbar^2}{2m} \frac{\partial^2}{\partial z^2} + \frac{\hat{\ell}^2}{2mr^2} \right] \otimes \hat{1} + \hat{H}_0, \quad (\text{S1})$$

where  $\hat{\ell} = -i\hbar\partial_\phi$  is the orbital angular momentum operator, and the atom-light coupling is

$$\begin{aligned} \hat{H}_0/\hbar = & e^{i\Delta\omega_L t} \frac{\Omega(r)}{\sqrt{2}} e^{i\phi} |1\rangle\langle 0| + e^{i\Delta\omega_L t} \frac{\Omega(r)}{\sqrt{2}} e^{i\phi} |0\rangle\langle -1| \\ & + e^{-i\Delta\omega_{\text{mw}} t} \frac{\Omega_{\text{mw}}}{2} e^{-i\theta_{\text{mw}}} | -1\rangle\langle 1| + \text{H.c.} \sum_{m_F=0,\pm 1} \omega_{m_F} |m_F\rangle\langle m_F|, \end{aligned} \quad (\text{S2})$$

$\Delta\omega_L, \Delta\omega_{\text{mw}}$  are the frequency differences between the two Raman laser beams and between two microwave fields, respectively. The  $|m_F\rangle$  spin state has energy  $\hbar\omega_{m_F}$  including the Zeeman energy shifts and the microwave-induced light shifts  $\delta\omega_{m_F}$ , where  $\omega_1 = -\omega_Z^{(0)} + \delta\omega_1, \omega_0 = -\omega_q^{(0)} + \delta\omega_0, \omega_{-1} = \omega_Z^{(0)} + \delta\omega_{-1}$ ;  $\omega_Z^{(0)}$  and  $\omega_q^{(0)}$  are the linear and quadratic Zeeman energy shift, respectively. We further define the effective Zeeman shift  $\omega_Z = (\omega_{-1} - \omega_1)/2$  and the effective quadratic Zeeman shift  $\omega_q = (\omega_{-1} + \omega_1)/2 - \omega_0$ . Then, we rewrite  $\omega_{m_F}$  by adding an energy offset, and express as

$$\hat{H}_0 = \hbar \begin{pmatrix} -\omega_Z & e^{i\Delta\omega_L t} \frac{\Omega(r)}{\sqrt{2}} e^{i\phi} & e^{i\Delta\omega_{\text{mw}} t} \frac{\Omega_{\text{mw}}}{2} e^{i\theta_{\text{mw}}} \\ e^{-i\Delta\omega_L t} \frac{\Omega(r)}{\sqrt{2}} e^{-i\phi} & -\omega_q & e^{i\Delta\omega_L t} \frac{\Omega(r)}{\sqrt{2}} e^{i\phi} \\ e^{-i\Delta\omega_{\text{mw}} t} \frac{\Omega_{\text{mw}}}{2} e^{-i\theta_{\text{mw}}} & e^{-i\Delta\omega_L t} \frac{\Omega(r)}{\sqrt{2}} e^{-i\phi} & \omega_Z \end{pmatrix}. \quad (\text{S3})$$

In our experiment, we set the microwave frequency difference  $\Delta\omega_{\text{mw}}$  equal to twice of the Raman frequency difference  $\Delta\omega_L$ ,

$$2\Delta\omega_L - \Delta\omega_{\text{mw}} = 0. \quad (\text{S4})$$

We then express  $\hat{H}_0$  in the frame rotating at  $\Delta\omega_L$ , which is the general form of  $V$  in our main text,

$$V = \hbar \begin{pmatrix} \delta & \frac{\Omega(r)}{\sqrt{2}} e^{i\phi} & \frac{\Omega_{\text{mw}}}{2} e^{i\theta_{\text{mw}}} \\ \frac{\Omega(r)}{\sqrt{2}} e^{-i\phi} & -\omega_q & \frac{\Omega(r)}{\sqrt{2}} e^{i\phi} \\ \frac{\Omega_{\text{mw}}}{2} e^{-i\theta_{\text{mw}}} & \frac{\Omega(r)}{\sqrt{2}} e^{-i\phi} & -\delta \end{pmatrix}, \quad (\text{S5})$$

where the Raman detuning  $\delta = \Delta\omega_L - \omega_Z$  and  $V$  is time-independent.

#### Raman dressed state light shift

We consider the case when the microwave coupling  $\Omega_{\text{mw}}$  is zero. These Raman beams introduce the coupling to the atoms in the frame rotating at frequency  $\Delta\omega_L$ ,

$$H_\Omega/\hbar = \frac{\Omega(r)}{\sqrt{2}} e^{i\phi} |1\rangle\langle 0| + \frac{\Omega(r)}{\sqrt{2}} e^{i\phi} |0\rangle\langle -1| \pm \delta | \pm 1\rangle\langle \pm 1| + \text{H.c.} = \vec{\Omega}_{\text{eff}}(\vec{r}) \cdot \vec{F}, \quad (\text{S6})$$

where  $\vec{F}$  is the vector of spin operators and  $\vec{\Omega}_{\text{eff}} = \Omega(r) \cos\phi \mathbf{e}_x - \Omega(r) \sin\phi \mathbf{e}_y + \delta \mathbf{e}_z$  with  $\delta$  being the Raman detuning and  $\Omega(r) = \Omega_M \sqrt{e} (r/r_M) e^{-r^2/2r_M^2}$  the Raman coupling strength. Here we ignore the quadratic Zeeman shift for  $\Omega_{\text{mw}} = 0, \omega_q^{(0)}/2\pi = 50$  Hz. Because  $H_\Omega$  dominates the spin-dependent part of the Hamiltonian, it is convenient to

introduce the dressed spin basis  $|\xi_{n=0,\pm 1}(\vec{r})\rangle$  defined by  $H_\Omega|\xi_n(\vec{r})\rangle = n|\vec{\Omega}_{\text{eff}}(\vec{r})||\xi_n(\vec{r})\rangle$ , where  $|\xi_n(\vec{r})\rangle$  is a normalized spinor part of the wave function. The overall spinor order parameter for atoms being loaded the the lowest energy dressed state is  $\varphi(\vec{r})|\xi_{-1}(\vec{r})\rangle$  with a scalar wave function  $\varphi(\vec{r})$ , and the eigenenergy is  $\Omega_{\text{eff},-1} = -|\vec{\Omega}_{\text{eff}}(\vec{r})|$ ,

$$\Omega_{\text{eff},-1} = -\sqrt{\Omega(r)^2 + \delta^2}. \quad (\text{S7})$$

The dressed state light shift for  $|\xi_{-1}\rangle$  is  $-\sqrt{\Omega(r)^2 + \delta^2} - (-|\delta|)$ , which is  $-\Omega(r)^2/2|\delta|$  for large  $|\delta|$  and is  $-\Omega(r)$  for  $\delta = 0$ . Thus, in our Raman dress state before the microwave is turned on, the dressed state light shift  $-\Omega(r)$  provides a ring-shaped potential.

## EXPERIMENTAL SETUP AND PROCEDURES

At the beginning of the experiment, we perform evaporative cooling on  $^{87}\text{Rb}$  atoms in the state  $|F, m_F\rangle = |1, -1\rangle$ , confined in a crossed optical dipole trap [S1] combined with a 767 nm blue-detuned sheet potential. The 767 nm light is provided by a Toptica TA pro system consisting of a narrow-linewidth master laser and a tapered amplifier. The sheet beam propagates along  $\mathbf{e}_y$  and has a Hermite-Gaussian  $\text{TEM}_{01}$  profile along  $\mathbf{e}_z$ , providing tight vertical confinement. In addition, the sheet beam introduces weak anti-trapping potentials along  $\mathbf{e}_x$  and  $\mathbf{e}_y$ .

We then adiabatically load a cloud of cold thermal atoms into the lowest energy spinor branch Raman-dressed state  $|\xi_{-1}\rangle$  [S1] with detuning  $\delta = 0$ . After loading, the atoms have temperature  $T \gtrsim T_c$ , where  $T_c$  is the BEC critical temperature. We continue evaporative cooling by reducing the dipole trap power to near zero over 0.3 s, yielding a condensate of  $N = (8 \pm 1) \times 10^4$  atoms in the Raman-dressed state. The dressed state light shift at  $\delta = 0$  provides a ring-shaped trapping potential in the  $xy$  plane. In addition, the crossed dipole trap provides transverse confinement with  $\omega_r/2\pi = 25$  Hz, and the overall trap frequency along  $\mathbf{e}_z$  is about 370 Hz.

The two Raman beams co-propagate along the  $\mathbf{e}_z$  direction: one is Gaussian (G), and the other is Laguerre-Gaussian (LG). Both beams operate at  $\lambda = 790$  nm, where the scalar light shifts from the D1 and D2 lines cancel. The LG and G beams have optical frequencies  $\omega_L$  and  $\omega_L + \Delta\omega_L$ , and are linearly polarized along  $\mathbf{e}_x$  and  $\mathbf{e}_y$ , respectively. The LG beam, generated using a vortex phase plate, carries a phase winding number 1 and has radial index zero. The foci of both beams are aligned near the BEC position along  $\mathbf{e}_z$ , with the G beam having a waist of  $\approx 200$   $\mu\text{m}$ . The LG beam center is nearly coincident with the dipole trap center at  $(r = 0, z = 0)$ , with an estimated deviation of  $\lesssim 2$   $\mu\text{m}$ .

In the torus system, we derive the effective Zeeman and quadratic Zeeman shifts by measuring microwave-induced differential light shifts between  $|m_F, m_F \pm 1\rangle$ ,  $\delta\omega_1 - \delta\omega_0, \delta\omega_{-1} - \delta\omega_0$  with microwave two-photon resonance spectroscopy. In the time sequence of turning on the microwave coupling, we ramp  $\Omega_{\text{mw}}, \omega_q$  with a weak quadratic function  $\Omega_{\text{mw}}/(2\pi \times 3.15 \text{ kHz}) = \omega_q/(2\pi \times 1.6 \text{ kHz}) = -0.14f^2 + 1.14f$  for  $0 \leq f = t/t_{\text{on}} \leq 1$ ; the simultaneous ramp of bias field compensates the light shifts of microwave coupling such that the detuning  $|\delta/2\pi|$  is within  $\sim 150$  Hz.

We use a microwave field to selectively pump the atoms from  $|F = 1, m_F\rangle$  to  $|F = 2\rangle$  and perform resonant absorption imaging of  $F = 2 \rightarrow F' = 3$  transition. Each  $|m_F\rangle$  image is obtained in an individual experimental realization. All the images shown in the paper are single-shot.

In our experiments, several factors can contribute to cylindrical asymmetry. For a BEC centered at  $(r = 0, z = 0)$ , both Raman beams can be slightly misaligned in the transverse  $xy$  plane or have focal positions shifted along  $\mathbf{e}_z$ , introducing additional phase shifts due to the curvature of their wavefronts. The blue-detuned 767 nm sheet beam also produces a weak anti-trapping potential in the  $xy$  plane, with different curvatures along  $\mathbf{e}_x$  and  $\mathbf{e}_y$ . Additionally, we observe that the ring trap profile varies with the current of the 767 nm master laser, while the laser remains single frequency mode with fixed optical power. This suggests the presence of additional, unmodeled potentials from the sheet beam can break cylindrical symmetry.

## EXPERIMENTAL DATA ANALYSIS

Our experimental and simulation data of the atomic OD are in cartesian coordinate in discrete pixels. We first use an interpolation to obtain  $\text{OD}(x, y)$  for continuous variables  $(x, y)$ , and then analyze the data in cylindrical coordinate  $(r, \phi)$ .

The true 1D atomic density of spin  $m_F$  state is given by

$$n_{m_F}^{\text{1D}}(\phi - \theta_{\text{mw}}/2) = \int dr r n_{m_F}^{\text{2D}}(r, \phi - \theta_{\text{mw}}/2) = \bar{\sigma}^{-1} \int dr r \text{OD}_{m_F}(r, \phi - \theta_{\text{mw}}/2), \quad (\text{S8})$$

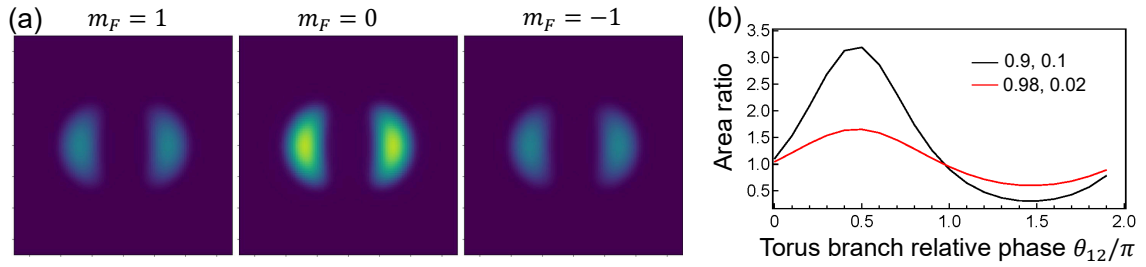


FIG. S1: (a) Optical density profiles of the torus in branch 1 for the ideal system with a perfect cylindrical symmetry. Branch 2 has identical density profiles as branch 1. (b) The area ratio  $r_a$  as a function of the relative phase  $\theta_{12}$  in the mixing of the two ground state branches of the torus. Branch mixtures of (0.9, 0.1) and (0.98, 0.02) are displayed.

where the 2D density  $n_{m_F}^{2D} = \bar{\sigma}^{-1} \text{OD}_{m_F}$  is given by the atomic OD and the imaging cross section  $\bar{\sigma}$ . Since the 1D density  $n_{m_F}^{1D}$  is proportional to the integrated OD along  $r$ , we then define the effective 1D density as

$$\tilde{n}_{m_F}(\phi) = \frac{1}{A_0} \left[ \int_{\phi - \Delta\phi/2}^{\phi + \Delta\phi/2} d\phi' \right]^{-1} \int_{\phi - \Delta\phi/2}^{\phi + \Delta\phi/2} d\phi' \int_r dr \text{OD}(r, \phi'), \quad (\text{S9})$$

where the OD is integrated within the azimuthal angle  $\phi - \Delta\phi/2 < \phi' < \phi + \Delta\phi/2$  and is averaged within the binning angle  $\Delta\phi$ , and  $A_0$  is the area of a single pixel. The pixel sizes are  $1.2 \mu\text{m}$  for experimental data and  $0.5596 \mu\text{m}$  for simulations, and the typical binning angle is  $\Delta\phi = 0.056\pi$ .

## NUMERICAL SIMULATIONS

Gross–Pitaevskii simulations included in this section were produced by Prof. Y. Yan at The Chinese University of Hong Kong, who has generously shared with us his results related to a previous work [S2].

### Torus branches and their mixing

In the ideal case of a cylindrically symmetric system, where the Raman beams and the resulting ring trap are perfectly symmetric and centered on the BEC, imaginary-time propagation was used to compute the 3D Gross–Pitaevskii (GP) ground states of the torus for branches 1 and 2 at  $\ell = 0$ , denoted as  $|\Phi_1\rangle$  and  $|\Phi_2\rangle$ , respectively [S2]. Since the energy  $E_0 \approx h \times 0.3 \text{ Hz}$  is much smaller than the Raman and microwave coupling strength, both branches have nearly the same spinor number fraction of (0.235, 0.529, 0.235) in  $m_F = (1, 0, -1)$  state. Both branches have the same density profile, as shown by the spinor optical density profiles of  $|\Phi_1\rangle$  in Fig. S1(a).

To gain further insight into the asymmetry between the two torus peaks observed in the experiment, in the GP simulations one needs to include possible misalignments of the Raman beams relative to the BEC center—an imperfection we believe to be a primary contributor. While it is difficult to account for all experimental sources of asymmetry (see Sec. “Experimental setup and procedures” for details on the setup), this modeled misalignment allows us to explore its impact. However, the simulated density profiles do not fully reproduce the asymmetries observed in the experiment. This discrepancy shows the challenge of faithfully capturing the experimental torus shapes in simulations, given the presence of uncontrolled or unmodeled imperfections.

Cylindrical asymmetry is one of the two factors that induces mixing between the two torus branches  $|\Phi_1\rangle$  and  $|\Phi_2\rangle$ . The amplitude of this mixing depends on the azimuthal structure of the external wave function  $\varphi(\vec{r})$  in the ring trap (before we turn on the microwave coupling), as well as on the microwave phase  $\theta_{\text{mw}}$ . Rather than focusing on the detailed ring trap potential, we examine the torus peak area ratio  $r_a$  from the azimuthal density profiles  $\tilde{n}_{m_F=1}$  as superpositions of  $|\Phi_1\rangle$  and  $|\Phi_2\rangle$  with varying weights and relative phases  $\theta_{12}$ , where  $r_a \neq 1$  indicates asymmetry between the two peaks. As shown in Fig. S1(b) with branch population fractions of (0.9, 0.1) and (0.98, 0.02), which correspond to mixing ratios of 10%, 2%, respectively, even a small admixture of the two branches can produce a noticeable asymmetry between the two density peaks—qualitatively consistent with experimental observations. The area ratio  $r_a$  oscillates with  $\theta_{12}$  and the maximum of  $r_a > 1$  increases with the mixing ratio. The 0.02 mixing ratio gives a similar range of  $r_a$  to that in the experiment.

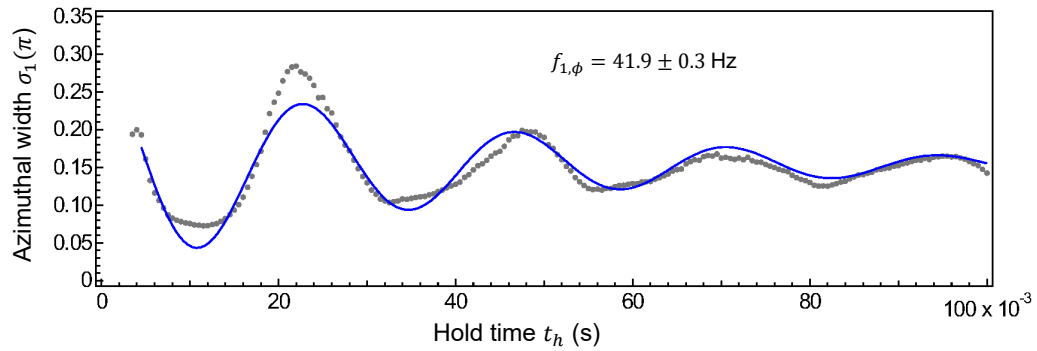


FIG. S2: Simulations of azimuthal width  $\sigma_1$  vs. hold time  $t_h$  after quench for a cylindrically symmetric system. Dark gray symbols (blue curve) denote the numerical data (fit). Unlike the experimental data in the main text, numerical results can well fit to a damped sinusoidal oscillation even at long times.

### Quench dynamics

The quench dynamics were simulated by solving the time-dependent Gross–Pitaevskii equation (TDGPE), assuming a perfectly cylindrically symmetric system for simplicity. The initial state is the GP ground state of Raman dressed state with  $\ell = 0$ , in the absence of the microwave field. At time  $t_h = 0$ , the microwave coupling  $\Omega_{\text{mw}}$  is suddenly turned on, loading the atoms into the torus branch 1. We track the evolution of the azimuthal root-mean-square widths  $\sigma_{1,2}$  of the torus peaks versus hold time  $t_h$  as torus features emerge, where we find  $\sigma_1 \approx \sigma_2$  as expected.

Figure. S2 shows  $\sigma_1$  as a function of  $t_h$ , along with a fit to a damped sinusoidal oscillation. While the fit shows some deviation from the numerical data, it yields a characteristic frequency of approximately 42 Hz. At short time  $t_h \lesssim 0.04$  s, the numerical results are close to the experimental data presented in Fig. 4 of the main text, showing similar oscillation frequencies. However, at longer  $t_h$ , the irregular dynamics observed in the experiment are no longer captured by the TDGPE simulation and cannot be well fit by a damped sinusoidal oscillation. This discrepancy suggests that a complete understanding of the quench dynamics requires more sophisticated studies of branch mixing, cylindrical asymmetries, and beyond mean-field effects in the system.

---

\* Electronic address: [zhou753@purdue.edu](mailto:zhou753@purdue.edu)

† Electronic address: [linyj@as.edu.tw](mailto:linyj@as.edu.tw)

[S1] P.-K. Chen, L.-R. Liu, M.-J. Tsai, N.-C. Chiu, Y. Kawaguchi, S.-K. Yip, M.-S. Chang, and Y.-J. Lin, *Phys. Rev. Lett.* **121**, 250401 (2018).

[S2] C.-H. Li, Y. Yan, S.-W. Feng, S. Choudhury, D. B. Blasing, Q. Zhou, and Y. P. Chen, *PRX Quantum* **3**, 010316 (2022).